J Adv Ceram

Research Article

High toughness and strong microwave absorption of layered Si_3N_4–SiC/BN ceramics loaded with different SiC contents

Erlin Zhao[1,2], Yi Jia[1,2], Quan Li[1,2,✉], Jianhao Zhang[1,2], Wenzhi Hao[1,2], Yang Wang[1,2], Jian Yang[1,2]

Cite this article: Zhao E, Jia Y, Li Q, et al. *J Adv Ceram* 2026, **15**(6): 9221310. https://doi.org/10.26599/JAC.2026.9221310

ABSTRACT: Layered ceramics can simultaneously achieve high toughness and strong microwave absorption. In this work, layered Si_3N_4–SiC/boron nitride (BN) ceramics were prepared by tape casting and hot pressing, and the effect of microsized SiC content on their mechanical and microwave absorption properties was investigated. The results show that the microsized SiC content has little effect on the mechanical properties of layered Si_3N_4–SiC/BN ceramics. All layered ceramics exhibited excellent mechanical properties, with flexural strengths exceeding 600 MPa and apparent fracture toughness exceeding 20 MPa·m$^{1/2}$. The layered ceramics containing 30 wt% SiC showed the best attenuation within the X-band (8.2–12.4 GHz), with a minimum reflection loss (RL) of −51.3 dB and an effective absorption bandwidth (EAB) of 0.84 GHz. Simulations show that superlayered architectures composed of layered ceramics loaded with different SiC contents can further improve microwave absorption, with the designed bilayer structure achieving an RL_{min} of −34 dB and an EAB of 3.2 GHz in the X-band. This work lays a foundation for further optimization and fabrication of high-performance microwave absorption ceramics via structural design.

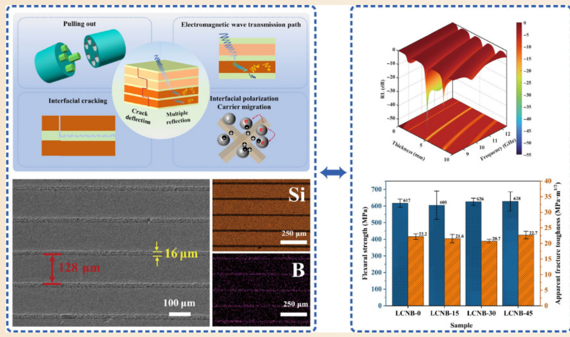

KEYWORDS: Si_3N_4–SiC/boron nitride (BN); layered ceramics; microwave absorption ceramics; high toughness

1 Introduction

High-density Si_3N_4–SiC ceramic-based microwave absorbers feature low density, high strength, high hardness, excellent oxidation stability, high temperature stability, and tunable dielectric properties [1–3]. These advantages allow them to operate in demanding thermal environments. However, these ceramic-based absorbers generally present narrow absorption bandwidths, with performance mainly determined by composition [4]. Moreover, their inherent brittleness and limited fracture energy still make them vulnerable to failure under impact or dynamic loading [5,6]. Enhancing both toughness and microwave absorption performance remains a key challenge for ceramic-based absorbing materials.

The layered architecture provides an effective strategy for enhancing the toughness of ceramic materials. In nature, nacre achieves a remarkable strength–toughness synergy through its alternating hard and soft layers [7–9], inspiring the introduction of weak interfaces and optimized layer-thickness ratios in engineered layers. Clegg *et al.* [10] first developed SiC/C layered ceramics with a fracture toughness of 15 MPa·m$^{1/2}$, which is nearly five times that of monolithic SiC. Since then, various layered ceramic systems have been developed, and their toughness improvements have been clearly demonstrated. Wei *et al.* [11] reported a fracture toughness of 13.5 MPa·m$^{1/2}$ for layered Si_3N_4/SiC_w ceramics. Shen *et al.* [12,13] reported a fracture toughness of 13.51 MPa·m$^{1/2}$ for layered Si_3N_4/boron nitride (BN) ceramics and 17.04 MPa·m$^{1/2}$ for layered Si_3N_4/TiN ceramics. These results indicate that well-designed interfaces and layered architectures can markedly enhance the fracture toughness of ceramic materials. However, current research on layered ceramics focuses on mechanical properties, with a lack of studies on microwave absorption performance. Si_3N_4/BN acts as a wave-transparent material, making it unsuitable for absorption. Regarding the Si_3N_4/TiN system, the high electrical conductivity of TiN leads to strong electromagnetic reflection. This makes the material function as an electromagnetic shielding agent rather than an absorber. SiC is a lossy semiconductor, making it a promising candidate for microwave absorption agents. Therefore, a Si_3N_4–SiC/BN layered system is proposed to synergize mechanical reliability and microwave absorption.

In terms of microwave absorption, achieving broadband performance requires proper impedance matching and adequate electromagnetic attenuation [14]. The fabrication of layered ceramics involves tape casting, lamination, and hot pressing. Tailoring the content of microwave-absorbing agents in the tape

[1] College of Materials Science and Engineering, Nanjing Tech University, Nanjing 211816, China. [2] Jiangsu Collaborative Innovation Center for Advanced Inorganic Function Composites, Nanjing Tech University, Nanjing 211816, China.

✉ Corresponding author. E-mail: quan@njtech.edu.cn

Received: January 6, 2026; Revised: March 30, 2026; Accepted: April 28, 2026

enables the fabrication of layered ceramics with a range of dielectric properties. Thus, impedance matching and microwave attenuating layered ceramics can be fabricated. Through tape stacking, superlayered architecture ceramics comprising both impedance-matching layered ceramics and microwave attenuating layered ceramics can be constructed to achieve broadband microwave-absorbing properties. Therefore, based on the above analysis, superlayered architecture ceramics can achieve both high toughness and broadband microwave absorption.

Layered ceramics consist of alternating matrix and interfacial layers, and both the composition and distribution of microwave absorption agents and geometric factors (e.g., the layer-thickness ratio) affect their mechanical and electromagnetic absorption properties. These factors have not been carefully disclosed, which brings difficulties to the design of high-performance superlayered ceramics. In this study, layered Si_3N_4–SiC/BN ceramics were fabricated. The effects of the microsized SiC content in the matrix layers on the mechanical properties and microwave absorption properties were first investigated. The obtained layered ceramics have excellent mechanical properties. Simulations also indicated that superlayered ceramics broaden the microwave absorption bandwidth. This work provides a foundation for developing high-performance ceramics with both high toughness and broadband microwave absorption in the future.

2 Materials and methods

2.1 Materials and processing

The raw materials used in this study included silicon nitride powders (Si_3N_4, α-phase content ≥ 93 wt%, D_{50} = 0.7 μm; Hebei Gaofu Silicon Nitride Materials Co., Ltd., China), silicon carbide powders (SiC, particle size 1–3 μm, 99.9% purity; Anhui Zhonghang Nano Technology Co., Ltd., China), yttrium oxide (Y_2O_3, 99.9% purity, particle size 0.5–1 μm; Qinhuangdao Yinuo High-Tech Materials Development Co., Ltd., China), aluminum oxide (Al_2O_3, 99.9% purity, D_{50} = 0.5 μm; Qinhuangdao Yinuo High-Tech Materials Development Co., Ltd., China), and hexagonal BN (purity 99%, D_{50} = 0.5 μm; Qinhuangdao Yinuo High-Tech Materials Development Co., Ltd., China). A mixed solvent of absolute ethanol and isopropanol with a volume ratio of 1:1 was employed. Triethyl phosphate (TEP) was used as the dispersant, polyvinyl butyral (PVB) served as the binder, and a plasticizer mixture of glycerol and diethyl phthalate (DEP) was used at a volume ratio of 1:1.

As illustrated in Fig. 1, layered Si_3N_4–SiC/BN ceramics were fabricated through tape casting and hot pressing. The matrix layers were composed of Si_3N_4 with varying SiC contents, while the interfacial layers consisted of BN with 20 wt% Si_3N_4. Subsequently, the binder and plasticizer were incorporated, followed by an additional 10 h of ball milling to achieve complete homogenization. The resulting slurry was subsequently degassed under vacuum for 15 min to remove entrapped air. Tape casting was carried out on a laboratory-scale casting unit with a casting speed of 0.25 m/min and a drying temperature of 30 °C. The doctor blade gap was set to 300 μm for the matrix-layer slurries and 150 μm for the interfacial-layer slurries. After drying, the green tapes showed average thicknesses of 85 μm for the matrix layers and 36 μm for the interfacial layers. They were then cut into 67 mm × 64 mm sheets. The green tapes were alternately stacked at a matrix-to-interfacial layer ratio of 4:1 until a total layer thickness of approximately 2 cm was obtained. Debinding was performed at 600 °C for 2 h in a nitrogen atmosphere, followed by an oxidation step at 600 °C for 12 h in air using a muffle furnace (KSL1700X-A2, Hefei Kejing Material Technology Co., Ltd., China) to remove residual carbon derived from the organics. Final densification was achieved by hot pressing at 1850 °C for 1 h under a uniaxial pressure of 30 MPa in nitrogen. The SiC content in the matrix layers was set at 0, 15, 30, and 45 wt%, with the corresponding layered ceramic specimens designated LCNB-0, LCNB-15, LCNB-30, and LCNB-45, respectively. Layered ceramics with low SiC content exhibit good impedance matching, while those with high SiC content provide significant electromagnetic loss capacity. The content range used in this work allows for the selection of impedance matching layers and lossy layers. These functional layers provide the foundation for constructing superlayered ceramics.

2.2 Material characterization

The phase composition of the ceramic samples was analyzed using an X-ray diffractometer (XRD; Regulus 8100, Hitachi, Japan) under 30 kV Cu Kα radiation. The morphology and microstructure of the composite materials were characterized using a scanning electron microscope (SEM; JEM-7600F, JEOL, Japan). Prior to SEM observation, samples were polished and subsequently etched with molten NaOH for 1 min. The relative permittivity of the ceramic materials was measured at room temperature using the waveguide method in the X band (8.2–12.4 GHz) with a vector network analyzer (N5244A, Agilent, USA). The reflection loss (RL) was calculated by Eq. (1) [15]:

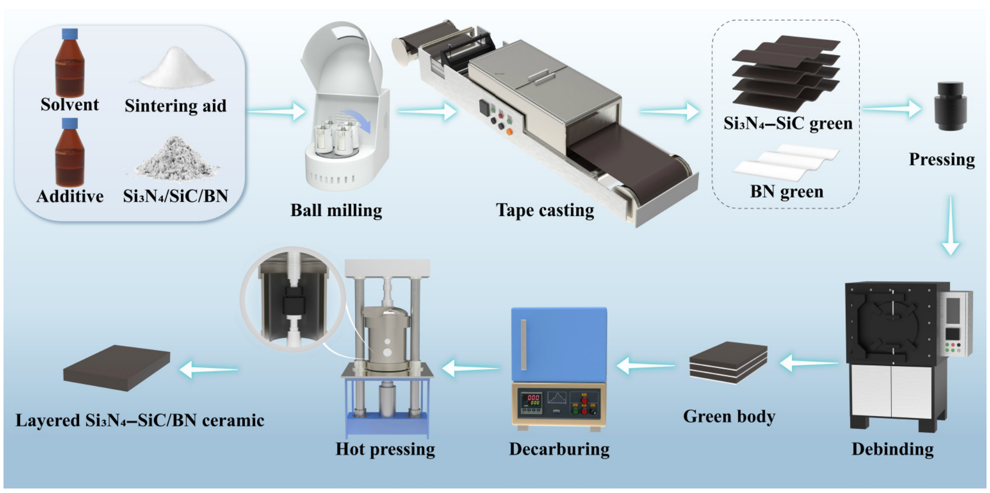

Fig. 1 Preparation of layered Si_3N_4–SiC/BN ceramics via tape casting and hot pressing.

$$\mathrm{RL(dB)} = 20\log\left|\frac{Z_{in} - Z_0}{Z_{in} + Z_0}\right| \tag{1}$$

where Z_{in} is the input impedance of the absorber, and Z_0 is the free-space impedance (377 Ω). The input impedance is determined from the classical metal back-panel model, as shown in Eq. (2):

$$Z_{in} = Z_0\sqrt{\frac{\mu_r}{\varepsilon_r}}\tanh\left(j\frac{2\pi fd}{c}\sqrt{\mu_r\varepsilon_r}\right) \tag{2}$$

where μ_r and ε_r are the relative permeability and permittivity, f is the frequency, d is the sample thickness, and c is the speed of light. Since all constituent phases (Si_3N_4, SiC, and h-BN) are intrinsically nonmagnetic, the real and imaginary parts of the magnetic permeability of the layered ceramic are 1 and 0, respectively. The input impedance ratio (Z_r) and the attenuation constant (α) are employed to characterize the impedance matching and attenuation capability of the absorber, respectively. Z_r is defined as Eq. (3) [16]:

$$Z_r = \left|\frac{Z_{in}}{Z_0}\right| \tag{3}$$

When Z_r approaches 1, good impedance matching is achieved, allowing the incident electromagnetic waves to efficiently enter the absorber. The energy dissipation capability inside the material is evaluated by α, which is expressed as Eq. (4) [17]:

$$\alpha = \frac{\sqrt{2}\pi f}{c} \times\sqrt{(\mu''\varepsilon'' - \mu'\varepsilon') + \sqrt{(\mu''\varepsilon'' - \mu'\varepsilon')^2 + (\mu''\varepsilon' + \mu'\varepsilon'')^2}} \tag{4}$$

where ε', ε'', μ', and μ'' are the real and imaginary parts of the permittivity and permeability, respectively. A larger α implies stronger electromagnetic energy dissipation within the absorber. Flexural strength is tested using a three-point bending test with a specimen strip of 40 mm × 4 mm × 3 mm at a span of 30 mm and a speed of 0.5 mm/min. Fracture toughness is measured with a single-edge notched beam (SENB) test using a 30 mm × 4 mm × 2 mm strip, a span of 20 mm, and a speed of 0.05 mm/min. The loading direction is perpendicular to the layered structure, as shown in Fig. 2.

Fracture toughness (K_{IC}) can be calculated using Eq. (5) [18]:

$$K_{IC} = \frac{P}{B}\frac{S}{W^{\frac{3}{2}}}f\left(\frac{a}{W}\right) \tag{5}$$

In Eq. (5), the function $f(a/W)$ can be specifically expressed as Eq. (6):

$$f\left(\frac{a}{W}\right) = 2.9\left(\frac{a}{W}\right)^{1/2} - 4.6\left(\frac{a}{W}\right)^{\frac{3}{2}} + 21.8\left(\frac{a}{W}\right)^{\frac{5}{2}} - 37.6\left(\frac{a}{W}\right)^{\frac{7}{2}} + 38.7\left(\frac{a}{W}\right)^{9/2} \tag{6}$$

where P is the maximum load, B the width of the test piece, S the support span, W the thickness of the test piece, and a the notch length.

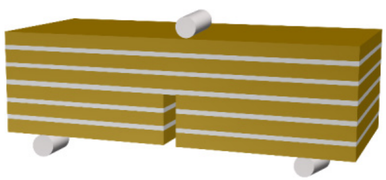

Fig. 2 Schematic illustration of loading direction in SENB fracture toughness test.

3 Results and discussion

3.1 Phase compositions and microstructures

As shown in Fig. 3, the diffraction pattern of the SiC-free sample (LCNB-0) is dominated by the characteristic peaks of β-Si_3N_4, indicating that the α→β phase transformation was nearly complete during hot pressing at 1850 °C. This result agrees with previous studies reporting that sintering above approximately 1750 °C facilitates the full conversion of α-Si_3N_4 into the thermodynamically stable β-Si_3N_4 phase [19,20]. In SiC-containing samples (LCNB-15, LCNB-30, and LCNB-45), α-Si_3N_4 peaks are also not detected, confirming that SiC addition has little effect on the α→β transformation of Si_3N_4 under hot pressing conditions at 1850 °C. In these samples, the characteristic diffraction peaks of SiC appear at $2\theta \approx$ 35.6°, 41.36°, and 59.9°. Notably, both 3C-SiC and 6H-SiC polytypes can be identified at these positions, indicating the coexistence of multiple SiC polytypes and possible polytype evolution at high temperature. The diffraction peak intensity of SiC significantly increases with higher SiC content, while the peaks of β-Si_3N_4 relatively weaken. This change in diffraction intensity indicates a notable increase in the relative content of crystalline SiC and a corresponding decrease in β-Si_3N_4, which is consistent with the designed layered compositions. Weak hexagonal boron nitride (h-BN) peaks are also observed in all samples, which are assigned to the BN in the interfacial layers.

Figure 4 displays the SEM images of the layered samples. The low-magnification SEM images (Figs. 4(a1)–4(d1)) and element distributions of Si and B (Figs. 4(a5)–4(d6)) confirm the successful construction of a periodic layered architecture, which is composed of two distinct regions: the matrix layers and the interfacial layers. For the LCNB-0 sample, the average matrix-layer thickness is approximately 117 μm, whereas for all SiC-containing samples (LCNB-15, LCNB-30, and LCNB-45), it increases to approximately 128 μm. The BN-rich interfacial layers remain consistent across all compositions, with an average thickness of approximately 16 μm. The overall architecture is highly ordered and free of interfacial delamination or through-thickness porosity, demonstrating the high precision of the tape-casting and hot pressing processes.

As shown in Table 1, the layered ceramics prepared in this study exhibit a bulk density of 3.04–3.06 g·cm^{-3}, corresponding to a relative density of approximately 93%. This indicates that the

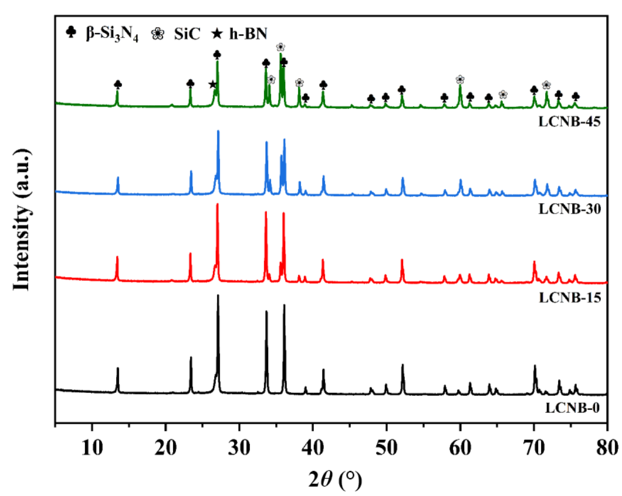

Fig. 3 XRD patterns of layered Si_3N_4–SiC/BN ceramic samples loaded with different SiC contents in Si_3N_4–SiC matrix layer.

https://doi.org/10.26599/JAC.2026.9221310

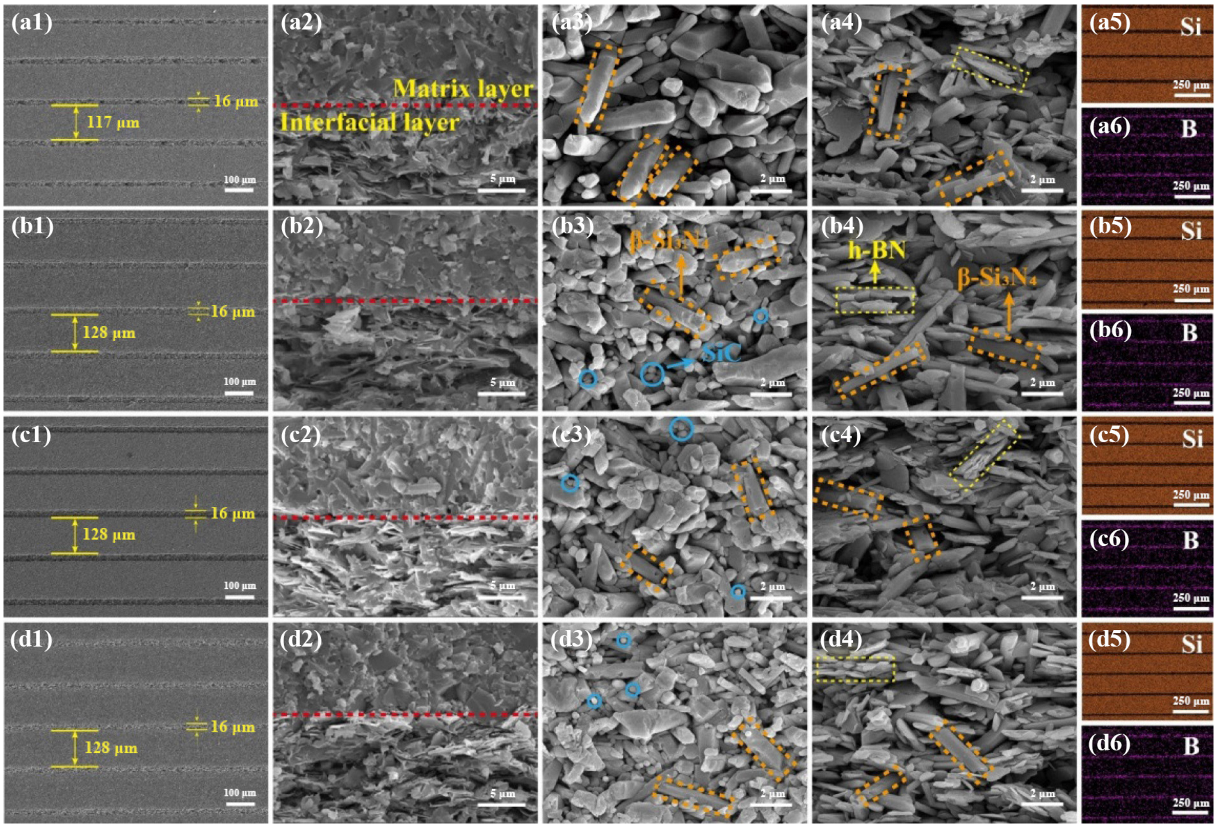

Fig. 4 Microstructural analysis of layered Si_3N_4–SiC/BN ceramics with varying SiC contents: (a) LCNB-0, (b) LCNB-15, (c) LCNB-30, and (d) LCNB-45. (a1–d1) As-polished cross-sectional SEM images at low magnification; (a2–d2) as-polished SEM images of matrix/interfacial region; (a3–d3) SEM images of NaOH-etched Si_3N_4–SiC matrix layers; (a4–d4) SEM images of NaOH-etched BN-rich interfacial layers; (a5–d5) elemental mapping of Si; (a6–d6) elemental mapping of B.

Table 1 Bulk density, relative density, and apparent porosity of layered Si_3N_4–SiC/BN ceramics with different SiC contents

Sample	Bulk density (g/cm^3)	Relative density (%)	Apparent porosity (%)
LCNB-0	3.06	93.51	0.44
LCNB-15	3.04	92.92	0.32
LCNB-30	3.04	93.05	0.61
LCNB-45	3.06	93.71	0.43

material has achieved a high level of overall densification. As shown in Figs. 4(a2)–4(d2), the matrix layers are composed of densely packed Si_3N_4 grains with well-bonded grain boundaries and very few residual pores, indicating effective densification during hot pressing. The interfacial layers display a characteristic lamellar BN structure with a loosely stacked morphology, where visible interfacial layer gaps act as the main source of porosity in the layers. To examine the densification and porosity of the matrix and interfacial layers, Si_3N_4–SiC (30 wt%) and BN–Si_3N_4 (20 wt%) composite ceramics were prepared, and their densities and relative densities were measured. The Si_3N_4–SiC composite has a relative density of 97.63%, while the BN–Si_3N_4 composite shows a much lower relative density of 75.65%. This indicates that the BN-based interfacial layer acts as the main pore-rich region in the layered structure. The microstructures observed in this work follow this trend and explain why the overall bulk density of the layered ceramics is slightly lower than that of fully dense Si_3N_4–SiC ceramics.

To elucidate the fine microstructure and distribution of the Si_3N_4, SiC, and BN phases, the samples were chemically etched with molten NaOH. The resulting SEM images are presented in Figs. 4(a3)–4(d3) and Figs. 4(a4)–4(d4). The etched matrix layers (Figs. 4(a3)–4(d3)) are predominantly composed of elongated β-Si_3N_4 grains. In the LCNB-0 sample, β-Si_3N_4 grains show a relatively coarse rod-like morphology, with an average grain length of approximately 3 µm and a diameter of approximately 1 µm. The SiC-containing samples (LCNB-15, LCNB-30, and LCNB-45) exhibit pronounced grain refinement. The β-Si_3N_4 grains in these samples have lengths mainly in the range of 1–2 µm and an average diameter of approximately 0.45 µm. The SiC phase appears as fine particles with an average size of approximately 0.3 µm dispersed along the Si_3N_4 grain boundaries, exerting a pronounced grain-boundary pinning effect. This pinning behavior effectively suppresses abnormal grain coarsening, resulting in the refinement and more uniform alignment of β-Si_3N_4 grains [21,22]. In all SiC-containing samples, the SiC phase is homogeneously distributed throughout the Si_3N_4–SiC matrix without observable agglomeration. In contrast, the BN-based interfacial layers shown in Figs. 4(a4)–4(d4) exhibit loosely stacked and partially oriented lamellae, which is a typical morphology of hexagonal BN. Fine rod-shaped Si_3N_4 grains are evenly dispersed among the BN lamellae, forming moderate interfacial bonding without disrupting the layered architecture. The morphology and thickness of the BN interfacial layers are nearly identical across all samples, indicating that SiC incorporation into the matrix has little influence on the formation or structural integrity of the BN-based interfaces.

3.2 Dielectric properties and microwave absorption properties

The complex permittivity ($\varepsilon_r = \varepsilon' - j\varepsilon''$) is a fundamental parameter describing the dielectric response of microwave absorbers. The ε' quantifies the capacity for electromagnetic energy storage, and ε'' represents dielectric energy dissipation. The dielectric loss tangent ($\tan\delta_\varepsilon = \varepsilon''/\varepsilon'$) is commonly adopted as an integrated metric for evaluating dielectric loss performance [23]. Figures 5(a)–5(c) show the values of ε', ε'', and $\tan\delta_\varepsilon$ of samples prepared with different SiC contents. The dielectric properties of the layered ceramics increase steadily with increasing SiC content, indicating that the dielectric response of the layered ceramics is strongly affected by the incorporation of SiC particles. LCNB-0 contains a pure Si_3N_4 matrix and behaves as an insulating material, so its dielectric constant and dielectric loss remain at the lowest level. Introduction of SiC in the matrix layer could result in numerous Si_3N_4–SiC heterogeneous interfaces, which enhance Maxwell–Wagner interfacial polarization [24]. During hot pressing, nitrogen from Si_3N_4 and the N_2 atmosphere dissolves into the transient liquid phase and enters the SiC lattice through a dissolution–reprecipitation process, producing N-doped SiC grains with higher carrier concentration and mobility [25]. The accompanying lattice defects and local distortions further contribute to defect polarization [26]. Therefore, as the SiC content increases from 0 to 30 wt%, ε' rises from 7.31 to 27.22 and ε'' increases from 0.04 to 2.07, reflecting a clear increase in interfacial and defect polarization. At this SiC content, partial contact between SiC particles creates short-range conductive paths, so conduction loss begins to play a role in the overall attenuation [25]. With the SiC content raised to 45 wt%, the particle contacts become more continuous, giving rise to a conductive network. As a result, conduction loss becomes one of the major contributors to the attenuation mechanism.

To assess the effect of the BN-based interfacial layers, the dielectric properties of the layered ceramics were compared with those of the monolithic Si_3N_4–SiC composite. Because BN, Si_3N_4, and the pores in the interfacial layers have low permittivity, the dielectric mixing rule predicts a decrease in ε'. Accordingly, the layered Si_3N_4–SiC/BN ceramics show a lower ε' than the Si_3N_4–SiC composite. For example, the layered sample LCNB-30 has an ε' of 27.22, while the monolithic Si_3N_4–SiC (30 wt%) composite has an ε' of 38.05. However, the introduction of the interfacial layers does not reduce ε'' or the dielectric loss. Instead, the layered Si_3N_4–SiC/BN ceramics show higher ε'' (≈ 2.07) and a higher $\tan\delta_\varepsilon$ (≈ 0.08) than the monolithic Si_3N_4–SiC composite (ε'' ≈ 1.44 and $\tan\delta_\varepsilon$ ≈ 0.04). This is probably caused by multiple reflections of microwaves at the interfaces between the matrix layers and the BN interfacial layers, which extend the microwave propagation path and increase energy dissipation.

The microwave absorption performance of a material is mainly determined by impedance matching and attenuation capability [27], which are largely controlled by the complex permittivity [28]. Strong absorption occurs only when a proper balance between these two factors is achieved. Figures 6 and 7 depict the evolution of Z_r, α, and the corresponding RL. Z_r was calculated at a fixed thickness of 2 mm. Because it has the lowest permittivity, LCNB-0 shows the best impedance matching, with Z_r approaching 1 in the X-band. However, its α remains very low, resulting in insufficient energy dissipation. Consequently, most microwaves transmit through it with minimal absorption. For LCNB-15, Z_r deviates markedly from 1 and shows a pronounced peak near 10 GHz, indicating severe impedance mismatch. Although α increases slightly compared with LCNB-0, the mismatched impedance restricts the penetration of incident electromagnetic waves into the material. Even at a thickness of 7.99 mm, the RL_{min} is merely

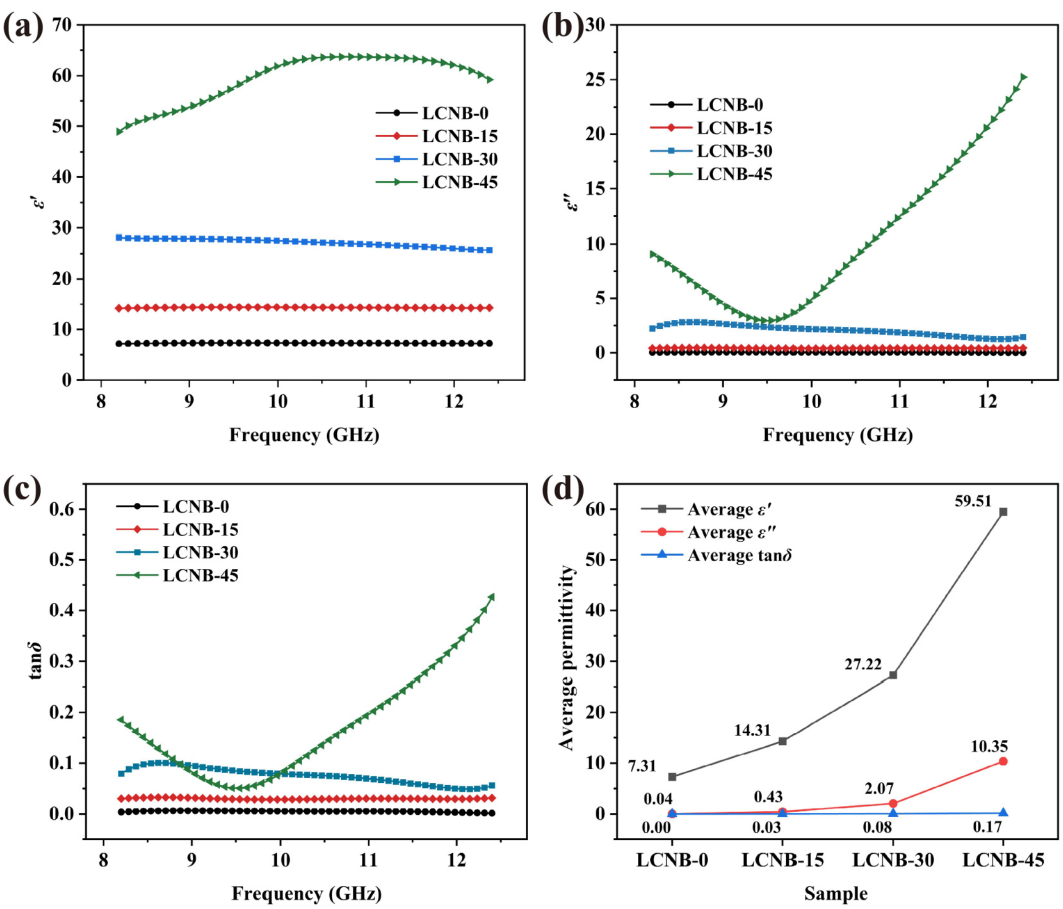

Fig. 5 (a) ε', (b) ε'', (c) $\tan\delta_\varepsilon$, and (d) average values of ε', ε'', and $\tan\delta_\varepsilon$ of layered Si_3N_4–SiC/BN ceramics with different SiC contents.

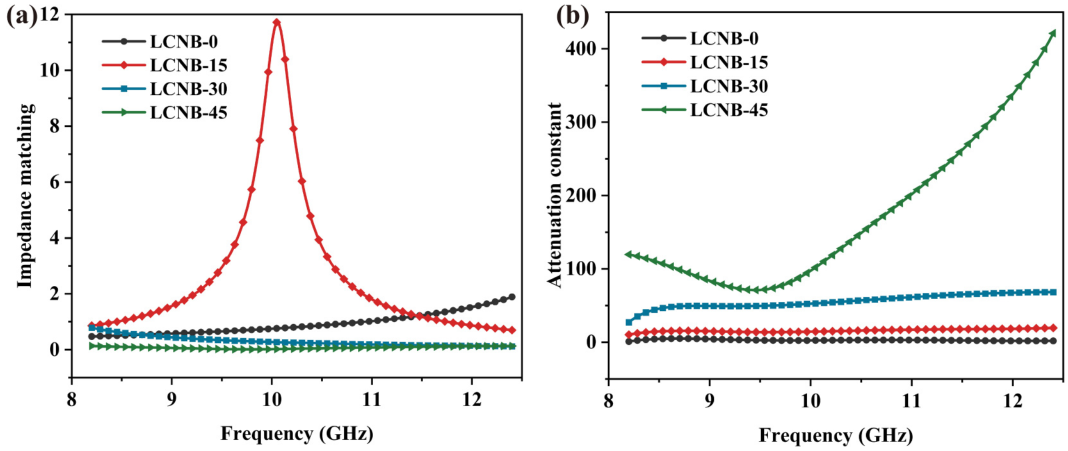

Fig. 6 (a) Impedance matching and (b) α of layered Si_3N_4–SiC/BN ceramics.

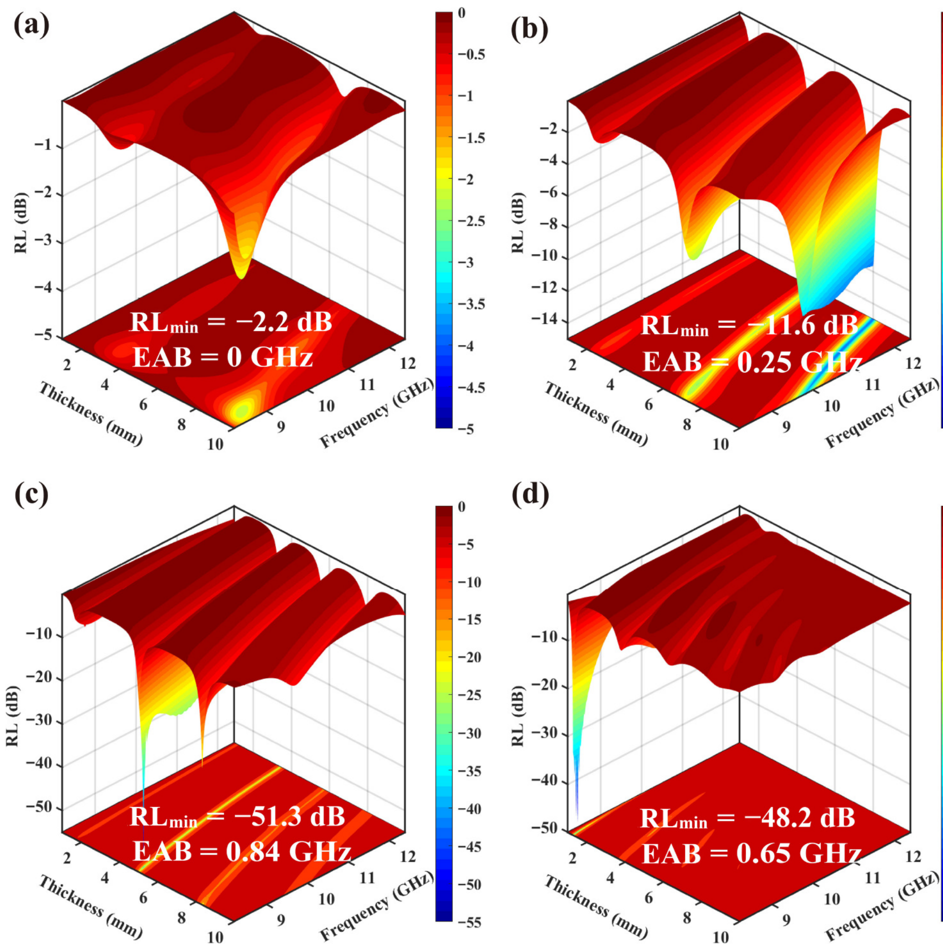

Fig. 7 RL of layered Si_3N_4–SiC/BN ceramics prepared with different SiC contents: (a) LCNB-0, (b) LCNB-15, (c) LCNB-30, and (d) LCNB-45.

−11.6 dB at 12.4 GHz. LCNB-30 and LCNB-45 exhibit better performance. Sample LCNB-30 achieves an RL_{min} of −51.3 dB at 8.4 GHz with an optimal thickness of 4.89 mm, while sample LCNB-45 shows an RL_{min} of −48.2 dB at 8.3 GHz with a thickness of 1.24 mm. This improvement results from an improved balance between Z_r and α of samples LCNB-30 and LCNB-45 compared to that of LCNB-0 and LCNB-15.

Although LCNB-30 and LCNB-45 achieve strong absorption, their effective absorption bandwidths (EABs) remain narrow. The EABs of LCNB-30 and LCNB-45 are 0.84 and 0.65 GHz, respectively. An advantage of the tape-casting process is its capability to tailor the layered architecture, enabling the integration of impedance-matching and lossy layers within a layered ceramic to broaden the absorption bandwidth. A bilayer absorber (a superlayered architecture composed of LCNB-0 and LCNB-45) was designed by combining an impedance-matching layer with a loss-dominated layer. As shown in Fig. 8, the LCNB-0 layer (2.4 mm) functions as an impedance-matching layer, while the LCNB-45 layer (8.2 mm) acts as a dielectric lossy layer. The simulation predicts an RL_{min} of −34.2 dB and an EAB of 3.2 GHz in the X-band, showing a clear improvement over the single-layer structures. However, the relatively low dielectric loss of the lossy layer (LCNB-45) limits the absorption bandwidth. The introduction of CNTs or SiC whiskers into the lossy layer could enhance the loss capacity of the layered ceramic and further broaden the absorption bandwidth of the superlayered architecture. In future work, this bilayer superlayered architecture will be fabricated and experimentally tested to verify the simulated performance, followed by thickness optimization of each functional layer to achieve broader-band absorption.

3.3 Mechanical properties

Figure 9 summarizes the mechanical properties of the layered

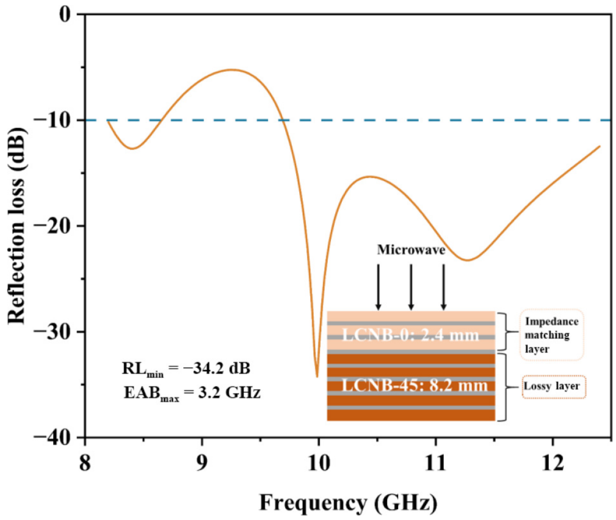

Fig. 8 RL curves of LCNB-0/LCNB-45 bilayer superlayered architecture obtained from multilayer simulation.

Si_3N_4–SiC/BN ceramics. Figure 9(a) shows the load–displacement curves obtained from single-edge notched beam (SENB) tests. All samples exhibit an initial linear elastic region, followed by a nonlinear stage prior to final failure. The curves display a distinct serrated pattern, which is characteristic of layered ceramic architecture. These serrations are attributed to repeated crack deflection and interfacial debonding during crack propagation. Such behavior indicates a noncatastrophic (or quasiductile) fracture mode, demonstrating that the multilayer design effectively arrests crack advancement and dissipates energy [29,30]. The flexural strength and apparent fracture toughness of the samples are presented in Fig. 9(b). The materials possess high flexural strengths, exceeding 600 MPa, and high apparent fracture toughness values, exceeding 20 $MPa{\cdot}m^{1/2}$. The achieved apparent fracture toughness is markedly higher than that of monolithic Si_3N_4 ceramics and is also superior to many reported ceramic matrix composites [31,32], such as SiC whisker-reinforced Si_3N_4 [33–35]. The work of fracture of the samples was also calculated using Eq. (7) [36]:

$$\gamma_{\text{wof}} = \frac{\int P\mathrm{d}\delta}{2A} \tag{7}$$

where γ_{wof} is the work of fracture, P is the applied load, δ is the displacement, and A is the cross-sectional area of the unnotched portion of the sample. As shown in Fig. 9(c), the work of fracture values of the four samples are 5459 J/m^2 (LCNB-0), 4817·J/m^2 (LCNB-15), 5002 J/m^2 (LCNB-30), and 4852 J/m^2 (LCNB-45). From the above analysis, all samples show comparable mechanical properties, suggesting that the content of microsized SiC in the matrix layers has a limited influence on the overall mechanical performance.

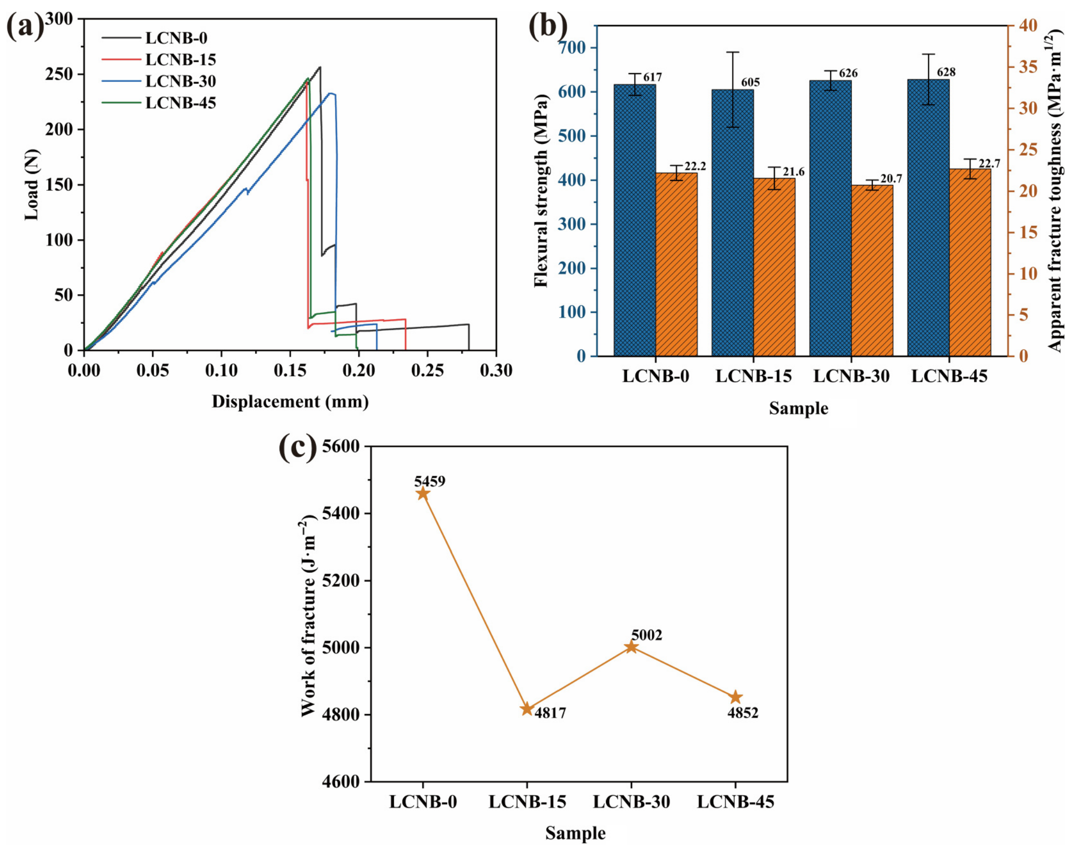

Fig. 9 (a) Load–displacement curves, (b) flexural strength and apparent fracture toughness, and (c) work of fracture of layered Si_3N_4–SiC/BN ceramics with different SiC contents.

The high apparent fracture toughness of the layered ceramics is attributed to the interfacial architecture. As shown in Figs. 4(a2)–4(d2), the BN-based interfacial layers exhibit a loose and porous structure. When the crack enters these regions, the crack tip becomes blunted by the pores and subsequently reorients along these features, resulting in interfacial cracking and local delamination (Figs. 10(a) and 10(b)) [37]. Therefore, as shown in Fig. 10(a), the main crack does not travel in a straight line but is repeatedly deflected at each BN interfacial layer, producing a step-like propagation path. This behavior indicates a moderate bonding strength between the matrix and the BN layers, which is sufficient to prevent premature delamination while still allowing interfacial sliding and crack deflection [38–40]. In addition, the Si_3N_4–SiC matrix layers (Fig. 10(c)) are highly densified and act as the primary load-bearing layers in the layered architecture. During fracture, the pull-out of high-aspect-ratio Si_3N_4 grains also dissipates fracture energy, further contributing to the apparent fracture toughness of layered samples.

Residual stresses caused by thermal expansion mismatch during cooling also influence crack propagation in the layers [41–43]. The residual stresses between the adjacent matrix and interfacial layers can be evaluated using Hsueh's formula, as shown in Eq. (8) [11]:

$$\sigma = \frac{E_0 E_1 (h_0 - h_1)(\alpha_1 - \alpha_0)\Delta T}{(1 - \nu_0)E_1 h_1 + (1 - \nu_1)E_0 h_0} \tag{8}$$

where ν, E, ΔT, and h denote Poisson's ratio, Young's modulus, temperature change (negative during cooling), and layer thickness, respectively. Subscripts 0 and 1 refer to the matrix and interfacial layers. Because h-BN has an in-plane thermal expansion coefficient far lower than those of Si_3N_4 and SiC, it contracts much less during cooling. This generates compressive residual stress in the BN interfacial layers. When a crack reaches the interface, the compressive stress reduces its opening tendency and favors crack deflection or interfacial sliding [44,45]. The resulting curved crack path requires more energy to extend, which helps enhance the fracture toughness of the layered ceramic.

The above analysis demonstrates that the layered architecture ceramics exhibit both high fracture toughness and excellent microwave absorption performance. The corresponding toughening and absorption mechanisms are summarized in Fig. 11. As illustrated in Fig. 11, the outstanding multifunctional performance of the layered Si_3N_4–SiC/BN ceramics results from the synergistic contribution of multiple mechanisms across different hierarchical levels. For microwave absorption, the impedance-matching layer first ensures the efficient entry of microwaves into the ceramic interior. The dispersed SiC particles in the Si_3N_4–SiC matrix create numerous heterogeneous interfaces that activate interfacial polarization under alternating fields. Electron hopping and tunneling between adjacent SiC particles further establish carrier transport pathways, leading to pronounced conduction loss. The periodic layered configuration further induces successive reflections and scattering at multiple interfaces, extending the effective propagation path and facilitating cumulative energy attenuation. These cooperative mechanisms jointly contribute to strong microwave absorption. For mechanical properties, the BN-rich weak interfaces act as preferential crack paths, triggering deflection, branching, and interfacial sliding under applied stress, effectively elongating the fracture trajectory and enhancing energy dissipation during crack propagation. Meanwhile, the densely elongated β-Si_3N_4 grains provide a robust load-bearing framework, with grain pull-out and frictional sliding contributing additional extrinsic toughening. Overall, the layered architecture integrates impedance-matching and crack-deflection effects from BN interfacial layers, interfacial polarization and carrier migration from SiC particles, and multireflection dissipation from the layered structure, thereby

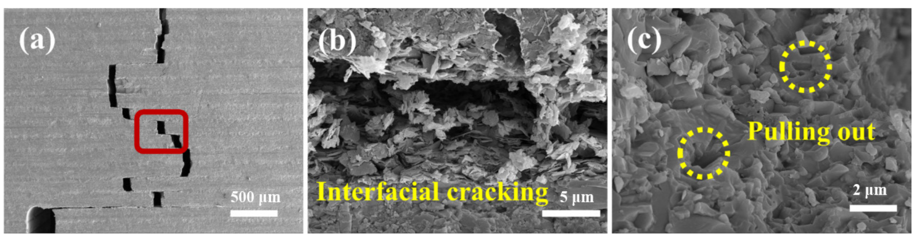

Fig. 10 Crack propagation morphologies of layered Si_3N_4–SiC/BN ceramics: (a) low-magnification crack path, (b) high-magnification fracture morphology of interfacial layer, and (c) high-magnification fracture morphology of matrix layer.

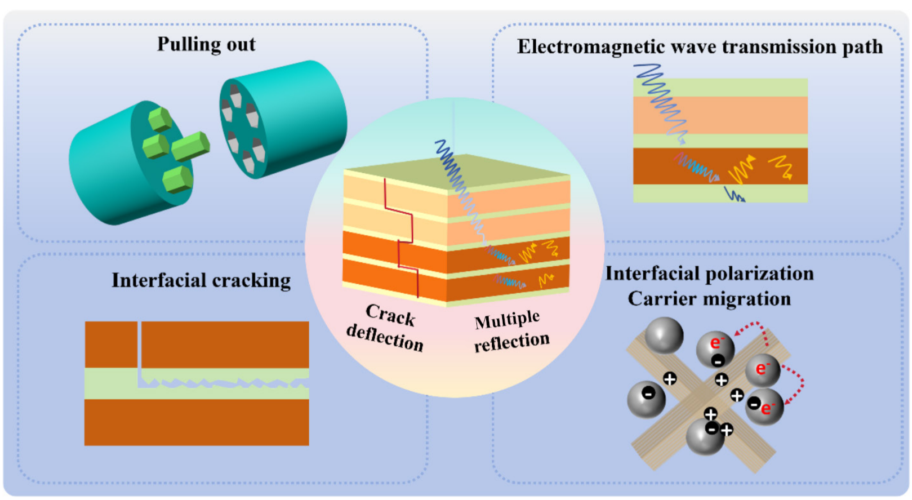

Fig. 11 Proposed mechanism of microwave absorption and fracture toughening in layered Si_3N_4–SiC/BN ceramics.

realizing a simultaneous enhancement of both mechanical reliability and microwave absorption.

Table 2 summarizes the mechanical properties and microwave absorption performance of various Si_3N_4-based ceramics reported in the literature and compares them with the results of this work. Most reported materials show either good mechanical performance or noticeable microwave absorption, but rarely both. In contrast, the monolithic layered Si_3N_4–SiC/BN ceramics developed in this study exhibit high flexural strength, high fracture toughness, and strong microwave absorption, with an RL_{min} of −51.3 dB. Although the EAB is still limited, a bilayer superlayered architecture further broadens the bandwidth.

Table 2 Comparison of mechanical properties and microwave absorption performance reported in literatures and this work

Sample	Flexural strength (MPa)	Fracture toughness ($MPa\cdot m^{1/2}$)	RL_{min} (dB)	EAB_{max} (GHz)	Ref.
Si_3N_4	712	7.7	—	—	[31]
Si_3N_4–SiC_f	357	10.8	—	—	[46]
Si_3N_4/SiC	564	16.8	—	—	[47]
Si_3N_4/BN	429	13.5	—	—	[12]
SiC_f/mullite	154	24.3	−30.3	4.20	[48]
Si_3N_4–SiC_w	939	9.4	−16.2	2.74	[34]
Si_3N_4–SiC_{nw}	240	3.7	−14.7	3.47	[35]
C_f-Si_3N_4	326	9.0	−19.6	2.23	[49]
LCNB-30	626	20.7	−51.3	0.84	This work
LCNB-45	628	22.7	−48.2	0.65	This work
Bilayer superlayered architecture	—	—	−34.2	3.20	This work (simulation)

4 Conclusions

This study successfully fabricated layered Si_3N_4–SiC/BN ceramics with strong microwave absorption and high flexural toughness and strength. For microwave absorption, the SiC particles introduced into the Si_3N_4 matrix activated interfacial polarization, defect polarization, and conduction loss. The periodic layered structure produced repeated interfacial reflections and scattering, which extended the propagation path of electromagnetic waves. Among all samples, LCNB-30 showed the strongest absorption, with an RL_{min} of −51.3 dB. In terms of mechanical properties, all layered ceramics exhibited high flexural strength (> 600 MPa) and high apparent fracture toughness (> 20 $MPa\cdot m^{1/2}$). Toughening resulted from crack deflection, interfacial sliding, local debonding within the BN layers, and β-Si_3N_4 grain pull-out, which together formed energy-dissipating crack paths. A superlayered architecture design combining LCNB-0 and LCNB-45 was developed. In this structure, LCNB-0 serves as a low-permittivity matching layer, while LCNB-45 acts as a high-loss attenuation layer. Simulations show that this bilayer superlayered architecture broadens the EAB to 3.2 GHz, demonstrating the potential of structural-compositional design for developing microwave-absorbing ceramics with high strength, high toughness, and broadband performance. Overall, the layered Si_3N_4–SiC/BN ceramics exhibit high mechanical reliability and stable microwave-absorbing performance, making them ideal candidates for a structural-functional integrated component.

Acknowledgements

We gratefully acknowledge partial financial support for this work from the National Natural Science Foundation of China (No. 52272064).

Availability of data and materials

The data that support the findings of this study are available from the corresponding author upon reasonable request.

Competing interests

The authors have no competing interests to declare that are relevant to the content of this article.

References

[1] Zhang HH, Liu H, Zhu M, *et al.* Selective microwave absorption of SiC–Si_3N_4 porous ceramics prepared by sacrificial template method. *Ceram Int* 2023, **49**: 27604–27613.

[2] Bai JL, Yao XM, Liu XJ, *et al.* Study on the high-temperature microwave absorption performance and mechanism of SiC nanowire-reinforced porous Si_3N_4 ceramics. *Materials* 2025, **18**: 4071.

[3] Tang KK, Long FH, Zhang FH, *et al.* Research progress on high-temperature-resistant electromagnetic wave absorbers based on ceramic materials: A review. *Nanomaterials-Basel* 2025, **15**: 268.

[4] Yang YJ, Fan XM, Tang S, *et al.* Microstructure, microwave absorbing and mechanical properties of SiC_f/Si_3N_4 composites containing frequency selective surface (FSS)-type fiber cloth. *Ceram Int* 2025, **51**: 64759–64767.

[5] Guo AF, Kong DK, Zhou XY, *et al.* Method for preparing damage-resistant 3D-printed ceramics via interior-to-exterior strengthening and toughening. *Addit Manuf* 2022, **60**: 103272.

[6] Andraskar ND, Tiwari G, Goel MD. Impact response of ceramic structures—A review. *Ceram Int* 2022, **48**: 27262–27279.

[7] Evers K, Falco S, Grobert N, *et al.* Nacre-like alumina with unique high strain rate capabilities. *J Eur Ceram Soc* 2020, **40**: 417–426.

[8] Saad H, Douillard T, Malchère A, *et al.* Toughening mechanisms in nacre-like alumina revealed by *in-situ* imaging of stress. *J Eur Ceram Soc* 2022, **42**: 6757–6761.

[9] Chen JQ, Wang WL, Sun XN, *et al.* Fabrication and mechanical properties of nacre-like alumina with addition of silicon nitride. *Ceram Int* 2022, **48**: 21520–21531.

[10] Clegg WJ, Kendall K, Alford NM, *et al.* A simple way to make tough ceramics. *Nature* 1990, **347**: 455–457.

[11] Wei CC, Liu Z, Wu Y, *et al.* Toughness and R-curve behaviour of laminated Si_3N_4/SiC_w ceramics. *Ceram Int* 2021, **47**: 18693–18698.

[12] Shen XH, Zhang LZ, Ren ZK, *et al.* Improvement of mechanical properties of bio-inspired layered Si_3N_4/BN ceramics. *Ceram Int* 2024, **50**: 18220–18226.

[13] Shen XH, Li TY, Zhang LZ, *et al.* Improvement of mechanical properties of biomimetic-layered Si_3N_4 ceramics with TiN as the interface layer. *Int J Ceram Eng Sci* 2025, **7**: 10248.

[14] Wang XL, Fan XM, Dong YP, *et al.* Honeycomb structure SiC_f/Si_3N_4 composite with broadband electromagnetic absorption performance under a wide temperature range. *J Eur Ceram Soc* 2025, **45**: 117205.

[15] Zou J, Li Q, Zhao EL, *et al.* Microwave absorption and infrared stealth capabilities of hot-pressed Si_3N_4/CNT ceramics tailored by CNT content. *Ceram Int* 2024, **50**: 27530–27539.

[16] Wang L, Cai ZX, Su L, *et al.* Bifunctional SiC/Si_3N_4 aerogel for highly efficient electromagnetic wave absorption and thermal insulation. *J Adv Ceram* 2023, **12**: 309–320.

[17] Du B, Wang SD, Guo LW, *et al.* Design and fabrication of ($Hf_{0.25}Zr_{0.25}Ta_{0.25}Nb_{0.25}$)C–SiC ceramics with improved microwave absorbing properties *via* PDC route. *J Adv Ceram* 2025, **14**: 9220998.

[18] Yin XW, He SS, Zhang LT, *et al.* Fabrication and characterization of a carbon fibre reinforced carbon–silicon carbide–titanium silicon carbide hybrid matrix composite. *Mater Sci Eng A-Struct* 2010, **527**: 835–841.

[19] Kim KA, Lysenkov AS, Petrakova NV, *et al.* Effect of hot-pressing temperature on the properties of Si_3N_4 ceramics with a low content of eutectic CaO–Al_2O_3 sintering additive. *Ceram Int* 2025, **51**: 49403–49409.

[20] Wang L, Wang LY, Hao ZD, *et al.* Microstructure and properties of silicon nitride ceramics fabricated by vat photopolymerization in combination with pressureless sintering. *Ceram Int* 2024, **50**: 10485–10496.

[21] Hu HL, Yao DX, Xia YF, *et al.* Fabrication and mechanical properties of SiC reinforced reaction-bonded silicon nitride based ceramics. *Ceram Int* 2014, **40**: 4739–4743.

[22] Yang H, Li Q, Wang Z, *et al.* Effect of graphene on microstructure and mechanical properties of Si_3N_4/SiC ceramics. *ES Mater Manuf* 2021, **12**: 29–34.

[23] Yue Y, Wang YX, Xu XD, *et al.* *In-situ* growth of bamboo-shaped carbon nanotubes and helical carbon nanofibers on $Ti_3C_2T_x$ MXene at ultra-low temperature for enhanced electromagnetic wave absorption properties. *Ceram Int* 2022, **48**: 6338–6346.

[24] Sun Y, Zhao L, Hu YL, *et al.* Dense Si_3N_4/SiC composite ceramics with enhanced mechanical and electromagnetic absorption using micron-sized powders via spark plasma sintering. *Ceram Int* 2025, **51**: 25673–25680.

[25] Li Q, Wang ZC, Wang Y, *et al.* Electromagnetic wave absorption properties of hot-pressed Si_3N_4–SiC ceramic nanocomposites. *Int J Appl Ceram Tec* 2023, **20**: 3754–3765.

[26] Sun L, Li Q, Zhao EL, *et al.* Tuning the dielectric and microwave absorption properties of hot-pressed Si_3N_4–SiC composite ceramics by controlling doping and microstructure. *Ceram Int* 2025, **51**: 63722–63733.

[27] Hou WB, Shi XH, Ding JH, *et al.* Symmetric gradient structured SiCnws modified SiC/Si_3N_4 composites toward enhanced thermal stability, absorption power and electromagnetic interference shielding. *Ceram Int* 2025, **51**: 32844–32855.

[28] Fang X, Jin YH, Ma HQ, *et al.* Dielectric and electromagnetic wave absorption properties of TiN/Al_2O_3 composite ceramics with TiN as high-efficiency absorbent. *Ceram Int* 2025, **51**: 12992–13002.

[29] Bermejo R, Danzer R. High failure resistance layered ceramics using crack bifurcation and interface delamination as reinforcement mechanisms. *Eng Fract Mech* 2010, **77**: 2126–2135.

[30] Sun MY, Bai YH, Li MX, *et al.* Structural design and energy absorption mechanism of laminated SiC/BN ceramics. *J Eur Ceram Soc* 2018, **38**: 3742–3751.

[31] Fan BB, Hu ZL, Zhao S, *et al.* Fabrication of Si_3N_4 ceramics with improved thermal conductivity by carbothermal reduction and two-step sintering. *J Am Ceram Soc* 2024, **107**: 7319–7330.

[32] Li SS, Chen HB, Wang WD, *et al.* Effects of Y_2O_3/MgO ratio on mechanical properties and thermal conductivity of silicon nitride ceramics. *Int J Appl Ceram Tec* 2022, **19**: 2873–2882.

[33] Zhao L, Hu YL, Sun Y, *et al.* Enhancing toughness and electromagnetic wave absorption of Si_3N_4 ceramics by SiC whiskers with various diameters. *Ceram Int* 2025, **51**: 32744–32753.

[34] Jing J, Zhao YJ, Saleam A, *et al.* High mechanical properties and microwave absorption performances of SiCw/Si_3N_4 ceramic composites. *J Mater Sci-Mater El* 2023, **34**: 1384.

[35] Yin S, Jiang YH, Su K, *et al.* Preparation, mechanical, dielectric and microwave absorption properties of hierarchical porous SiC_{nw}–Si_3N_4 composite ceramics. *J Eur Ceram Soc* 2022, **42**: 3820–3830.

[36] Bai YH, Zhang BX, Du HL, *et al.* Efficient multiscale strategy for toughening HfB_2 ceramics: A heterogeneous ceramic–metal layered architecture. *J Am Ceram Soc* 2021, **104**: 1841–1851.

[37] Ma J, Wang HZ, Weng LQ, *et al.* Effect of porous interlayers on crack deflection in ceramic laminates. *J Eur Ceram Soc* 2004, **24**: 825–831.

[38] Hwu KL, Derby B. Fracture of metal/ceramic laminates—II. *Crack growth resistance and toughness. Acta Mater* 1999, **47**: 545–563.

[39] Song JJ, Zhang YS, Fan HZ, *et al.* Design of interfaces for optimal mechanical properties in Al_2O_3/Mo laminated composites. *J Eur Ceram Soc* 2015, **35**: 1123–1127.

[40] Song JJ, Su YF, Fan HZ, *et al.* A novel design to produce high-strength and high-toughness alumina self-lubricated composites with enhanced thermal-shock resistance: Part I: Mechanical properties and thermal shock behavior of Al_2O_3/Mo–Al_2O_3 laminated composites. *J Eur Ceram Soc* 2017, **37**: 213–221.

[41] Behera AK, Rahaman MM, Roy D. A residual stress-dependent mixed-mode phase-field model: Application to assessing the role of tailored residual stresses on the mechanical performance of ceramic laminates. *Mech Mater* 2024, **188**: 104867.

[42] Sánchez-Herencia AJ, Baudín C. Ceramic laminates with tailored residual stresses. *Bol Soc Esp Ceram V* 2009, **48**: 311–320.

[43] Li SJ, Huang CZ, Liu HL, *et al.* FEM and experimental research on residual stress, crack propagation and toughening mechanisms of novel bionic ceramic cutting tools. *Mater Charact* 2025, **223**: 114875.

[44] Bermejo R, Danzer R. Failure resistance optimisation in layered ceramics designed with strong interfaces. *J Ceram Sci Technol* 2010, **1**: 15–20.

[45] Chen XW, Cheng GF, Yang JS, *et al.* Effects of interfacial residual stress on mechanical behavior of SiC_f/SiC composites. *J Adv Ceram* 2022, **11**: 94–104.

[46] Mo R, Ye F, Liu XF, *et al.* A high-temperature structural and wave-absorbing SiC fiber reinforced Si_3N_4 matrix composites. *Ceram Int* 2021, **47**: 8191–8199.

[47] Ye F, Liu SC, Hu SQ, *et al.* A route to increase fracture toughness of layered Si_3N_4/SiC composite using interlocked interfaces. *Ceram Int* 2015, **41**: 10331–10335.

[48] Pan HJ, Luo F, Ren ZW, *et al.* Effect of interface structure on microwave absorbing performance and oxidation behavior of SiC_f/mullite composites. *Ceram Int* 2024, **50**: 46530–46541.

[49] Zhou W, Long L, Li Y. Mechanical and electromagnetic wave absorption properties of C_f–Si_3N_4 ceramics with PyC/SiC interphases. *J Mater Sci Technol* 2019, **35**: 2809–2813.